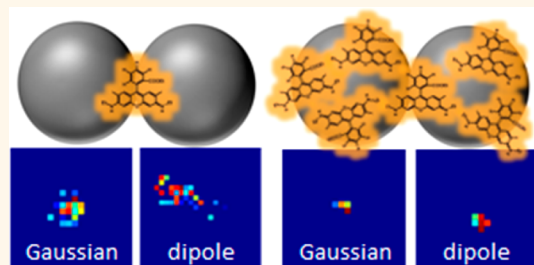


# Superlocalization Surface-Enhanced Raman Scattering Microscopy: Comparing Point Spread Function Models in the Ensemble and Single-Molecule Limits

Eric J. Titus and Katherine A. Willets\*

Department of Chemistry, The University of Texas at Austin, 105 E. 24th Street STOP A5300, Austin, Texas 78712, United States

**ABSTRACT** In this report, we compare the effectiveness of various dipole and Gaussian point spread function (PSF) models for fitting diffraction-limited surface-enhanced Raman scattering (SERS) emission images from rhodamine 6G-labeled nanoparticle dimers at both the high-concentration and single-molecule limit. Of all models tested, a 3-axis dipole PSF gives the best approximation to the experimental PSF, although none of the models utilized in the study were without systematic error when fitting the experimental data. In the high-concentration regime, all models localize the SERS emission to a stationary centroid position, with the dipole models providing additional orientation parameters that closely match the geometry of the dimer, indicating that the molecules are coupled to all resonant plasmon modes of the nanostructure. In the single-molecule case, the different models show a mobile SERS centroid, consistent with single-molecule motion on the surface, but the behavior of the centroid is model-dependent. Despite the centroid mobility in the single-molecule regime, the dipole PSF models still give accurate orientation information on the underlying dimer structure, although with less precision than the ensemble-averaged samples.



**KEYWORDS:** super-resolution imaging · point spread function · surface-enhanced Raman scattering · centroid · single molecule

Aggregation of plasmonic nanoparticles has long been recognized as a straightforward means to increase spectroscopic signals from molecules at or near the nanoparticle surface, by creating large electromagnetic field enhancements in the junction between adjacent nanoparticles.<sup>1–4</sup> In particular, aggregated nanoparticles have been critical for the observation of single-molecule surface-enhanced Raman scattering (SM-SERS), where the molecule is believed to be positioned somewhere in the gap between adjacent nanoparticles.<sup>4,5</sup> However, observing where individual molecules are located on the surface of nanoparticle aggregates is a distinct experimental challenge for two reasons. First, the SERS emission from the molecule(s) is not radiated directly into the far-field, but is instead coupled into and radiated by the nanoparticle substrate, leading to a

convolution between the position of the molecule(s) and the plasmon modes of the nanoparticle aggregate.<sup>6–8</sup> The second reason is that both the molecule(s) and the nanoparticles are smaller than the diffraction limit of light, which limits optical resolution to roughly half the wavelength of the emitted light.

Recently, super-resolution optical microscopy has been applied to problems in SM-SERS to overcome the diffraction limit of light and explore molecule–nanoparticle interactions.<sup>6,8–10</sup> In super-resolution microscopy, emission images are analyzed by fitting a theoretical emission point spread function (PSF) to the diffraction-limited emission pattern, in order to extract the center of emission, or centroid position, often with a precision of  $< 5$  nm.<sup>11,12</sup> The PSF is most commonly modeled as a two-dimensional Gaussian, due to its robustness

\* Address correspondence to [kwillets@cm.utexas.edu](mailto:kwillets@cm.utexas.edu).

Received for review July 26, 2013 and accepted August 28, 2013.

Published online August 28, 2013  
10.1021/nn403891t

© 2013 American Chemical Society

and low computational expense, where the centroid is defined as the location of the peak intensity. While this technique was initially developed for imaging fluorescent molecules, it has been successfully applied to understand the interactions between metal nanoparticles and molecules in studies of ligand binding,<sup>13,14</sup> catalysis,<sup>15</sup> and electromagnetic hot spots.<sup>8,10,16,17</sup> While the technique is starting to see a broader application in the field of plasmonics, the question of which theoretical PSF to use to fit the data remains.<sup>18</sup> In super-resolution studies of single molecule fluorescence, the orientation of the fluorophore can asymmetrically distort the PSF due to the dipolar emission of the molecule and its propagation through the sample–coverslip refractive index interface, creating a mismatch between the centroid position of the 2-D Gaussian fit and the actual position of the emitter.<sup>19–21</sup> To address this, dipole emission PSF models were developed that not only provide more accurate centroid localization (*i.e.*, the calculated centroid better matches the position of the emitter) but are also able to determine the orientation of the emitter at the interface; these models are further complemented by excitation beam-shaping approaches that allow for three-dimensional centroid localization, although this is beyond the scope of our work here.<sup>22–25</sup>

In the case of SERS-active nanoparticle dimers, most of the emission is coupled out through the longitudinal dipole plasmon mode of the nanostructure, suggesting that a dipole PSF might also be an appropriate model for fitting emission from these types of structures.<sup>26–29</sup> In previous work, we have shown excellent qualitative agreement between the SM-SERS emission from a nanoparticle dimer and a calculated dipole PSF based upon the three-dimensional orientation of that dimer.<sup>29</sup> Shegai *et al.* have shown similar qualitative agreement between a Fourier plane image of SERS emission from a nanoparticle dimer and a calculated dipole PSF, again using geometric parameters from the nanostructure to define the three-dimensional orientation of the calculated dipole emitter.<sup>28</sup> However, these studies have not attempted to actually fit the experimental emission pattern to a dipole PSF, which would not only provide a quantitative evaluation of the appropriateness of the dipole PSF model but also calculate the centroid position and the three-dimensional orientation of the best-fit dipole, which could then be compared to the actual nanoparticle structure. Such a study would be especially informative when comparing the emission patterns from SERS-active nanoparticle dimers in the regimes of both high analyte concentration (where we expect the SERS emission to couple to multiple resonant plasmon modes in the dimer, reducing the influence of the molecule on the PSF shape) and the single-molecule level (where the position of the molecule can impact plasmon coupling and therefore the site of the SERS emission).<sup>7,8</sup>

In the current study, we have applied a dipolar PSF fitting algorithm to model SERS emission from dye-labeled silver nanoparticle dimers to extract the centroid position, which represents the convolution between the molecular emission and the plasmon modes of the nanoparticle, while also potentially yielding geometric parameters associated with the SERS-active nanoparticle dimer. We have imaged dimers covered with a high concentration of SERS reporter dyes (multimolecule SERS, or MM-SERS) as well as SM-SERS-active nanoparticle dimers. In addition to fitting the experimental emission patterns to a single dipole PSF, we have also fit the data to the sum of three mutually orthogonal dipoles in order to account for other dipolar plasmon modes that may interact with the molecule on the surface. In previous work, we found that three dipole modes were necessary to provide the optimum fit—and thus best localization accuracy—to luminescence from gold nanorods, suggesting that a similar three-dipole approach might also be appropriate for these studies.<sup>30</sup> The various dipole PSF fits are compared to the standard 2-D Gaussian model in order to compare the fit centroids and precision between the different models.

## RESULTS AND DISCUSSION

Samples of silver nanoparticle dimer aggregates labeled with rhodamine 6G (R6G) (or its deuterated analogue, R6G-d4) were prepared, with the MM-SERS samples containing roughly 200 R6G molecules/aggregate and the SM-SERS samples containing roughly two dyes per aggregate; SM-SERS behavior was confirmed *via* on–off intensity fluctuations and a biaalyte approach (see SI section S2).<sup>31,32</sup> SERS emission images and spectra were collected simultaneously, in order to identify image frames that correspond to SERS activity (which is especially critical for SM-SERS, where signatures of either R6G or R6G-d4 alone were used to validate SM-SERS behavior). Dark-field scattering was used to measure the localized surface plasmon resonance (LSPR) of selected nanostructures after SERS imaging. The sample was then transferred to an atomic force microscope (AFM) coupled to an optical microscope in order to confirm that the nanoparticle aggregates are dimers and to determine their three-dimensional structure.

The 2-D Gaussian used for fitting SERS emission is shown in eq 1.

$$I(x, y) = z_0 + I_0 \exp \left[ -\frac{1}{2} \left[ \left( \frac{x - x_{0G}}{s_x} \right)^2 + \left( \frac{y - y_{0G}}{s_y} \right)^2 \right] \right] \quad (1)$$

Each experimental diffraction-limited image is fit to eq 1 to extract  $z_0$  (background intensity),  $I_0$  (peak intensity),  $x_{0G}$  and  $y_{0G}$  (the  $x$  and  $y$  Gaussian fit centroid positions, respectively), and  $s_x$  and  $s_y$  (the widths of the

Gaussian in the  $x$  and  $y$  directions, respectively), for a total of six fit parameters.<sup>6,8,10</sup> To generate the dipole PSF for the SERS fitting, we utilized a modified version of Jörg Enderlein's "QDControl.m" code, which is freely available online.<sup>33</sup> This algorithm generates a theoretical PSF based on a dipole emitter with up to three mutually orthogonal dipole components and calculates the PSF based on the dipole component strengths, the orientation and position of the emitter, and the dielectric environment and microscope imaging parameters. When fitting data to this model, we fix as many known or experimentally verifiable parameters as possible, including microscope magnification, numerical aperture (NA) of the objective, refractive index of the coverslip and immersion medium, detector pixel size, and coverslip thickness. The parameters that are fit (unless otherwise noted) include the microscope focus, the emission wavelength ( $\lambda$ ), the orientation of the longitudinal dipole mode ( $\varphi$  and  $\theta$ , see Figure 1), the dipole-fit centroid position of the dipole emission ( $x_{0D}$ ,  $y_{0D}$ ), the background and peak emission intensity, the distance of the emitter from the coverslip ( $z$ ), and the values  $\kappa$  and  $R$ , which define the relative contribution of each dipole axis component, as described below in eq 2.

$$I_{\text{total}} = R I_{\text{LM}} + (1 - R) \left( \frac{1 + \kappa}{2} I_{\text{TM}} + \frac{1 - \kappa}{2} I_{\text{OOP}} \right) \quad (2)$$

In eq 2,  $I_{\text{total}}$  represents the total dipole emission vector, and  $I_{\text{LM}}$ ,  $I_{\text{TM}}$ , and  $I_{\text{OOP}}$  represent unit vectors along each dipole axis (representing the longitudinal, transverse, and out-of-plane modes, respectively), as depicted in Figure 1. For nanoparticle dimers, the longitudinal plasmon mode is approximated as the line connecting the centers of the two nanoparticles, which is expected to dominate the SERS emission.<sup>26–29</sup> As shown in Figure 1A, the longitudinal mode is defined by the orientational parameters  $\varphi$  and  $\theta$ . We define the transverse dipole mode as perpendicular to the longitudinal mode and parallel to the plane of the coverslip, and the out-of-plane mode as perpendicular to both the longitudinal and transverse modes.

We began by looking at MM-SERS samples, where we expect the geometric features of the nanoparticle to dominate the emission pattern.<sup>28</sup> Figure 2 shows an example of a SERS-active dimer (Figure 2A) and its associated SERS emission pattern (Figure 2B). The emission pattern is dominated by a bright central lobe, but there are low-intensity side lobes oriented parallel to the long axis of the dimer, indicative of dipolar behavior.<sup>22,23,29,34</sup> Fitting the emission pattern to the 2-D Gaussian in eq 1 (Figure 2C), we find that this simple model fails to capture all of the features of the SERS emission pattern, particularly the low-intensity side lobes, as seen in the systematic error in the calculated residuals shown in Figure 2D.

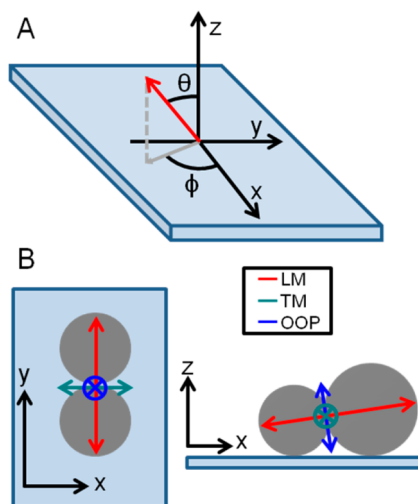


**Figure 1.** Orientation of axes used to define the dipole modes relative to the substrate. (A) Diagram showing how angles  $\varphi$  and  $\theta$  define the longitudinal dipole mode. (B) Diagrams showing the definition of the longitudinal (LM), transverse (TM), and out-of-plane (OOP) modes relative to nanoparticle structure. LM is estimated to lie along the center-to-center line of the nanoparticles.

Next, we fit the data to a single-axis dipole (fixing  $R = 1$  in eq 2 and assuming the emission originates at the surface,  $z = 0$ ), which we refer to as a one-dipole fit, shown in Figure 2E. In previous work, this model has shown excellent qualitative agreement between experimental emission patterns and a single-dipole PSF.<sup>28,29</sup> Qualitatively, the one-dipole fit better accounts for the shape of the experimental PSF, especially the low-intensity side lobes. We also obtain values for  $\varphi$  and  $\theta$  (Table 1), which show reasonable agreement with the orientation and out-of-plane tilt of the longitudinal mode of the SERS-active dimer, the estimation of which is based on a line connecting the nanoparticle centers (Figures 2A and 3A, respectively). However, the one-dipole fit also exhibits nonrandom residuals, as evidenced in Figure 2F. This observation is consistent with our recent study on gold nanorods, where a one-dipole fit was insufficient for modeling the PSF due to the presence of non-LM polarized emission.<sup>30</sup> Moreover, we find that the calculated emission wavelength of  $661 \pm 7$  nm is well to the red of both the SERS and the LSPR spectra of the sample (Figure 3B), indicating that this model is insufficient to capture all of the properties of the SERS emission from the nanoparticle dimer.

To account for the possibility of any emission coupling through the transverse or out-of-plane modes of the nanoparticle aggregate, a three-axis dipole model was used, in which both  $R$  and  $\kappa$  from eq 2 were included as fit parameters. For our first fit, we assumed a single emission wavelength, given that this model performed best when modeling luminescence from a gold nanorod, despite failing to capture the fact that the LM, TM, and OOP modes have different

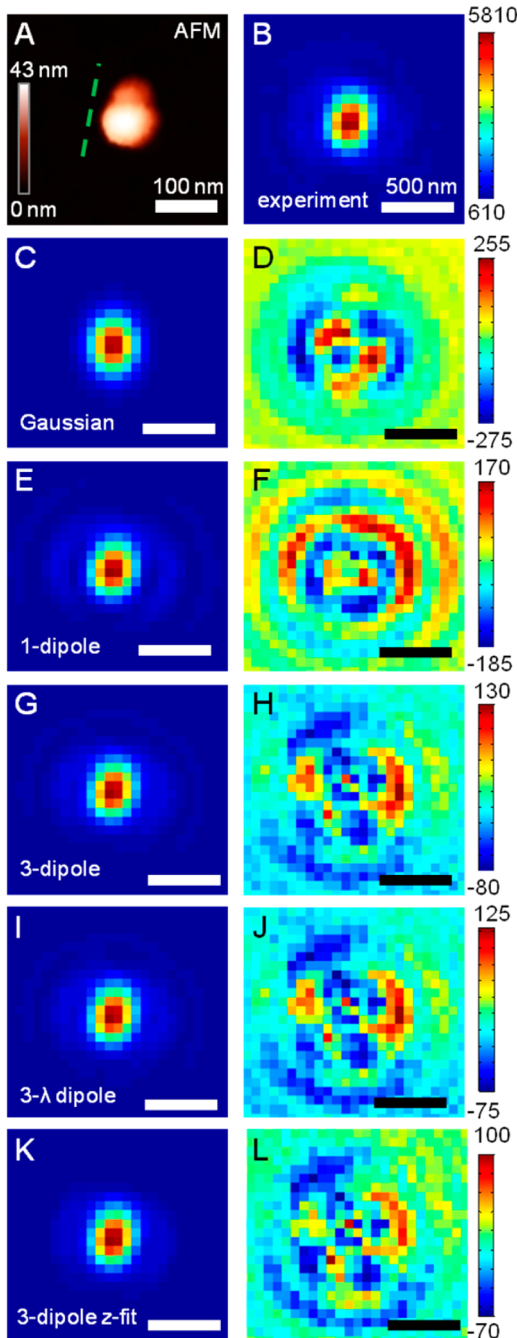


**Figure 2.** (A) AFM structure of nanoparticle dimer, where the green line indicates the  $\varphi$  value of the three-dipole fit. (B) Experimental MM-SERS intensity image. (C–L) Fits (left) and residuals (right) for the different PSF models as indicated.

resonances.<sup>30</sup> Figure 2G,H show the results of the fit and associated residuals, and we find that this model exhibits smaller residuals than the one-dipole and Gaussian fits, indicating that including contributions from each dipole axis is important in modeling the correct PSF. This model also provides values for  $\varphi$  and  $\theta$  (Table 1), which are in reasonable agreement with the geometry of the dimer (Figures 2A and 3A). However, the residuals in Figure 2H remain nonrandom, which tells us that this model is also imperfect at representing

the SERS emission from a nanoparticle dimer. This conclusion is further supported by the wavelength fit value of  $602 \pm 2$  nm, which is still more to the red than the bulk of the SERS emission as well as the LSPR maximum (Figure 3B).

Given that each dipole mode (LM, TM, and OOP) is expected to have a unique plasmon resonance, we next fit the data to a three-axis, three-wavelength dipole, where each dipole component has its own associated emission wavelength (denoted  $3\text{-}\lambda$  dipole, Figure 2I,J).<sup>1,2</sup> Interestingly, the residuals are nearly identical between the three-dipole (single- $\lambda$ ) fit in Figure 2H and the  $3\text{-}\lambda$  dipole fit in Figure 2J, showing that even if we allow the wavelengths to be fit independently, we do not observe a significant improvement in the overall quality of fit. Comparing the calculated emission wavelengths of the three dipole modes (Figure 3B), we find that both the TM and OOP modes are blue-shifted from the LM emission, as expected. However, the TM wavelength runs into our lower wavelength limit of 540 nm, which was set based on the cutoff wavelength of our long-pass filter. Moreover, the LM emission wavelength fit remains too far to the red of the actual emission, indicating that this model does not provide a significant improvement over the single- $\lambda$  analogue.

As a final test, we reran the three-dipole fit with a single emission wavelength, but this time included the distance of the emitter from the surface as a fit parameter (denoted three-dipole z-fit). We had set this value to  $z = 0$  for all previous fits, but we recognized that the emission might be offset from the surface, based on the geometry of the nanoparticle dimer. The fit and residuals for this model are shown in Figure 2K,L; again, we observe the same systematic error in the fit residuals, although the magnitude of the residuals is smaller than the other three-dipole cases. Interestingly, the emission wavelength that was fit using this model shows excellent agreement with the strongest SERS emission as well as the LSPR of the nanoparticle dimer (Figure 3B). Moreover, the calculated three-dimensional orientation once again agrees very well with the geometry of the nanoparticle dimer. However, we note that the surface offset,  $z$ , was fit to a value of  $74 \pm 8$  nm, which is larger than the actual height of the nanoparticles, as shown in Figure 3A. We also find that allowing the  $z$  value to be included as a fit parameter leads to nonconvergence of several of our fits (4 out of 20 frames do not converge). One possible explanation for this lack of convergence is the inclusion of too many fit parameters, which simply creates too large of a parameter space for our fits to ultimately reach a global minimum. However, we do not have this same convergence issue in the  $3\text{-}\lambda$  case, where we have two additional fit parameters over the case in which an offset is included. A second possible explanation for the poor convergence is that the model assumes that

**TABLE 1. Parameter Values for Different Fitting Functions Applied to the MM-SERS Example from Figure 2<sup>a</sup>**

	$\varphi$ (deg)	$\theta$ (deg)	$\lambda$ (nm)	$\Delta x$ (nm) <sup>b</sup>	$\Delta y$ (nm) <sup>b</sup>	fit time <sup>c</sup>	$R$	$K$	$z$
2-D Gaussian	N.A.	N.A.	N.A.	0.0(5)	0.0(4)	1 s	N.A.	N.A.	N.A.
1-dipole PSF	279.8(9)	77.6(6)	661(7)	1.9(5)	-10(1)	7 min	1 <sup>d</sup>	N.A.	0 <sup>d</sup>
3-dipole PSF (single- $\lambda$ )	280.0(9)	85.3(2)	602(2)	0.5(5)	-2.5(4)	15 min	0.82(2)	-0.7(1)	0 <sup>d</sup>
3-dipole PSF (multi- $\lambda$ ) <sup>e</sup>	281	83	597 (LM) 540 (TM) 586 (OOP)	0.8	-1.9	71 min	0.8	-0.05	0 <sup>d</sup>
3-dipole z-fit PSF	278(1)	83.3(5)	573(4)	0.0(5)	-0.3(4)	25 min	0.82(3)	-0.21(7)	74(8)

<sup>a</sup>Values in parentheses indicate the standard deviation of the fit in the last significant figure over 20 image frames. <sup>b</sup> $\Delta x$ ( $\Delta y$ ) corresponds to  $(x(y)_{0D} - x(y)_{0G})$  for each type of fit. <sup>c</sup>Per frame, approximate. <sup>d</sup>Fixed parameter. <sup>e</sup>Single frame fit.

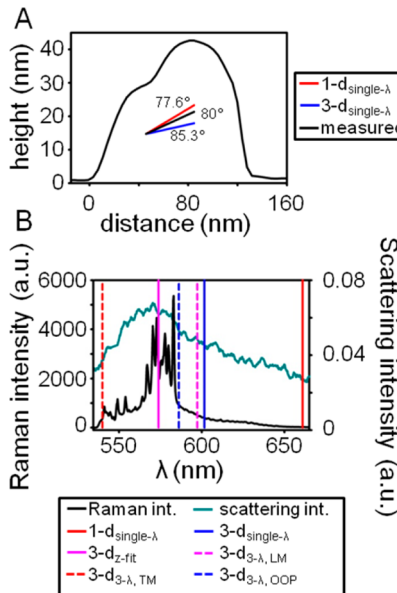


**Figure 3.** (A) AFM cross-section along the  $\varphi$  axis of the nanoparticle dimer from Figure 2. The red and blue lines show the  $\theta$  values from the one-dipole and three-dipole fits, with the black line indicating the measured  $\theta$  value. (B) Nanoparticle scattering (cyan) and Raman (black) spectra corresponding to the nanoparticle from Figure 2 with emission wavelength fit estimates overlaid. In the case of the 3- $\lambda$  dipole fit, each wavelength is represented separately.

the emission is traveling through a uniform refractive index environment (air) from its offset height  $z$  to the coverslip surface, which is most likely a naive assumption given the presence of the silver nanoparticle at the surface, as well as the possible presence of condensed water due to ambient humidity, both of which could introduce aberrations in the experimental emission pattern and discrepancies in the resulting fit.<sup>31</sup>

The results of the different fits used on this MM-SERS sample are compiled in Table 1. For all of the dipole fits, the  $\varphi$  values are within several degrees of each other and agree well with the orientation of the longitudinal axis of the dimer. The  $\theta$  values show slightly more variation, although they converge near the measured  $\theta$  value of 80°, as shown in Figure 3A. Thus, the various dipole fits perform reasonably well in predicting geometric parameters for the MM-SERS case. Moreover, all

of the three-dipole fits show  $R$  values of  $\sim 0.8$ , indicating that the bulk of the emission ( $\sim 80\%$ ) is dominated by the longitudinal dipole mode, as expected.

The results of a 2-D Gaussian fit are presented in the top row of Table 1 for comparison, and the average Gaussian centroid position is set to 0 in both  $x$  and  $y$ , with all other dipole centroid positions reported relative to this centroid (i.e.,  $\Delta x = x_{0D} - x_{0G}$ ,  $\Delta y = y_{0D} - y_{0G}$ ). While there is variation in the calculated centroid positions, we observe that the worst agreement with the Gaussian centroid occurs for the one-dipole case, which we also found was a poor model for representing the data. For the three-dipole z-fit model, we find that the centroid position actually agrees (within error) with the Gaussian, which is encouraging given that this model also yielded the best wavelength agreement. However, as discussed above, this model also yielded a nonphysical value for the surface offset, had poor convergence statistics, and is computationally expensive. The single and multiwavelength variants of the three-dipole fit both show a slight shift from the Gaussian centroid, with calculated distances of 2.5 and 2.1 nm, respectively. Previous work has shown that as  $\theta$  decreases from 90°, the calculated distance between the Gaussian and dipole centroids increases.<sup>19–21,30</sup> Interestingly, for our previous gold nanorod work, we found that a  $\theta$  value of 85° (as calculated here for the three-dipole fit) would lead to a centroid shift of nearly 10 nm between the Gaussian and three-dipole models, well above what is calculated here.<sup>30</sup> Thus, we find a much smaller difference between the centroid positions determined using the Gaussian and three-dipole models for the MM-SERS emission, compared to other plasmon-mediated emission processes. Lastly, we note that in all cases where multiple image frames were fit, the standard deviation in the centroid position is  $\leq 0.5$  nm (except for the one-dipole model), indicating that the SERS centroid is immobile in the MM-SERS regime.

We next proceed to an SM-SERS sample, which should allow us to observe the effect of the molecule on the PSF, given that the position of the molecule dictates how the emission couples to the different plasmon modes.<sup>6,27,35</sup> Figure 4 compares the fits and

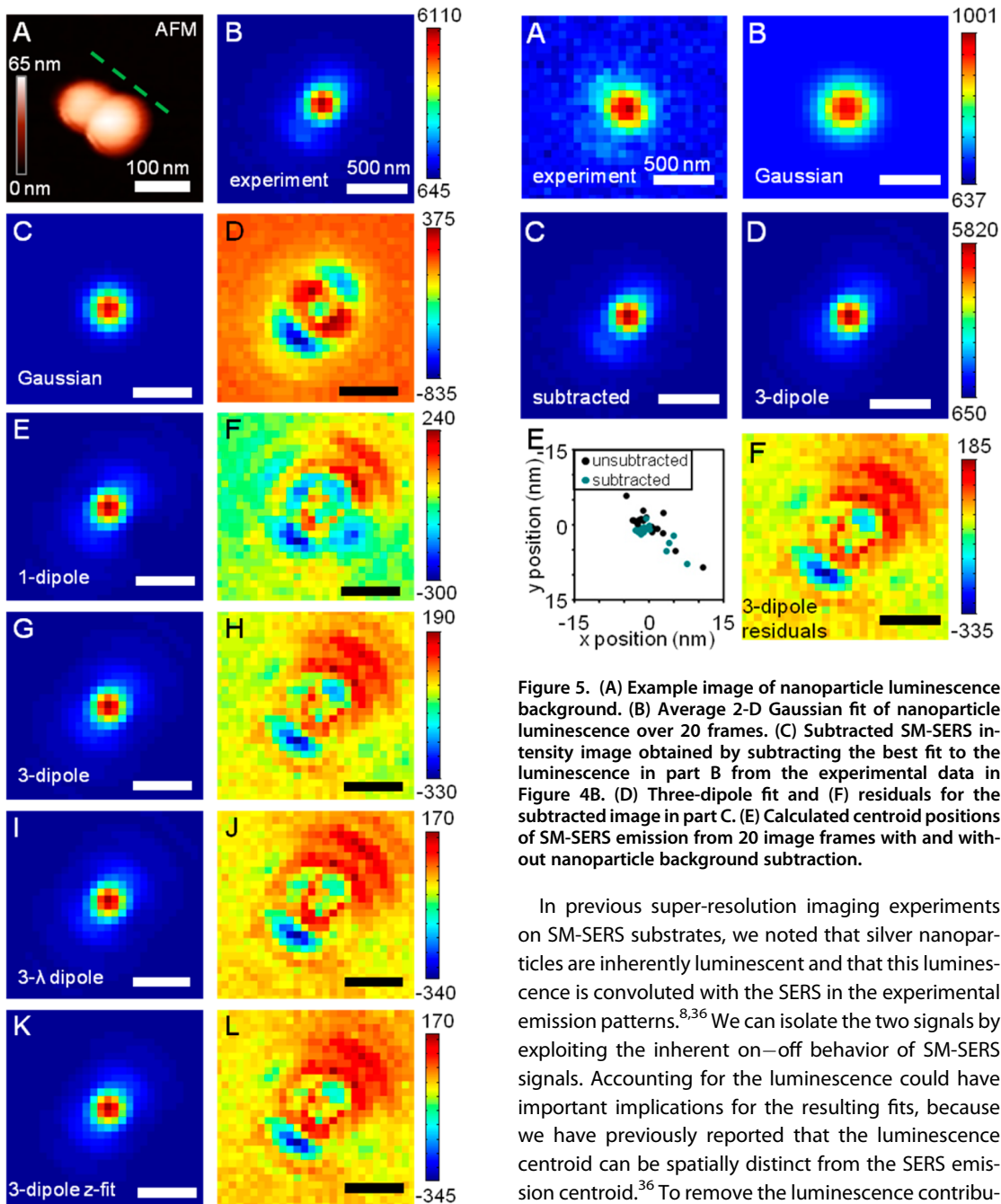


Figure 4. (A) AFM structure of nanoparticle dimer, where the green line indicates the  $\varphi$  value of the three-dipole fit. (B) Experimental SM-SERS intensity image. (C–L) Fits (left) and residuals (right) for the different PSF models as indicated.

residuals of the Gaussian and dipole fits on the SM-SERS-active nanoparticle dimer shown in Figure 4A, and we again see that the residual values shrink as we move from a 2-D Gaussian to a one-dipole fit and then improve incrementally as we apply the three-dipole,  $3\lambda$  dipole, and three-dipole z-fit models. As in the MM-SERS data presented in Figure 2, all of the fit residuals are nonrandom, indicating that these models are still not sufficient to capture the entirety of the SERS PSF.

Figure 5. (A) Example image of nanoparticle luminescence background. (B) Average 2-D Gaussian fit of nanoparticle luminescence over 20 frames. (C) Subtracted SM-SERS intensity image obtained by subtracting the best fit to the luminescence in part B from the experimental data in Figure 4B. (D) Three-dipole fit and (F) residuals for the subtracted image in part C. (E) Calculated centroid positions of SM-SERS emission from 20 image frames with and without nanoparticle background subtraction.

In previous super-resolution imaging experiments on SM-SERS substrates, we noted that silver nanoparticles are inherently luminescent and that this luminescence is convoluted with the SERS in the experimental emission patterns.<sup>8,36</sup> We can isolate the two signals by exploiting the inherent on–off behavior of SM-SERS signals. Accounting for the luminescence could have important implications for the resulting fits, because we have previously reported that the luminescence centroid can be spatially distinct from the SERS emission centroid.<sup>36</sup> To remove the luminescence contribution, we first use our correlated spectra to identify images when no SERS is observed and nanoparticle luminescence is the only contributor; an example is shown in Figure 5A. We use a 2-D Gaussian to fit each of the images associated with nanoparticle luminescence and then calculate an average best fit to represent the contribution from the nanoparticle, as shown in Figure 5B. Given the poor signal-to-noise of the luminescence, the more complex dipole models did not perform well, generating random and incorrect values of  $\varphi$ , which is why we used the 2-D Gaussian model to fit the luminescence images. Next, we subtract away the fitted luminescence contribution from the experimental emission image shown in Figure 4B to yield the isolated SM-SERS emission pattern shown in

**TABLE 2. Parameter Values for Different Fitting Functions Applied to the SM-SERS Example from Figure 4,<sup>a</sup>**

	$\varphi$ (deg)	$\theta$ (deg)	$\lambda$ (nm)	$\Delta x$ (nm) <sup>b</sup>	$\Delta y$ (nm) <sup>b</sup>	fit time <sup>c</sup>	$R$	$K$	$z$
2-D Gaussian	N.A.	N.A.	N.A.	0(2)	0(2)	1 s	N.A.	N.A.	N.A.
1-dipole PSF	39(2)	70(2)	630(12)	28(3)	25(4)	13 min	1 <sup>d</sup>	N.A.	0 <sup>d</sup>
3-dipole PSF (single- $\lambda$ )	38(1)	89(3)	603(7)	1(4)	4(3)	33 min	0.79(4)	0.0(2)	0 <sup>d</sup>
3-dipole PSF (multi- $\lambda$ ) <sup>e</sup>	37.6(9)	85(1)	611(5) (LM) 793(8) (TM) 780(30) (OOP)	4(1)	7(2)	137 min	0.84(1)	0.97(4)	0 <sup>d</sup>
3-dipole z-fit PSF <sup>e</sup>	38(2)	85(2)	584(6)	6(2)	8(2)	26 min	0.92(4)	0.8(3)	80(12)
bkgd-subtracted 3-dipole PSF <sup>e</sup>	38(2)	89(2)	603(8)	1(3)	5(2)	17 min	0.83(3)	-0.1(3)	0 <sup>d</sup>

<sup>a</sup> Values in parentheses indicate the standard deviation of the fit in the last significant figure over 31 image frames (except for lines marked with *e*). <sup>b</sup>  $\Delta x(\Delta y)$  corresponds to  $(x(y))_{00} - x(y)_{00}$  for each type of fit. <sup>c</sup> Per frame, approximate. <sup>d</sup> Fixed parameter.

Figure 5C. This image is then fit to the three-dipole model (Figure 5D), and the residuals are calculated (Figure 5F). We find that the residuals are nearly identical between the fits to the subtracted image (Figure 5F) and the nonsubtracted image (Figure 4H). However, if we compare the centroid positions that we calculate using either the raw image data or the subtracted image (Figure 5E), we find that the difference in average centroid position between the two cases is 1.7 nm. Although this offset is statistically significant as determined *via* a paired *t* test (at  $\alpha = 0.05$ ), we do not apply the luminescence subtraction for the rest of our SM-SERS analysis due to the lack of residual improvement.

Table 2 compares the fit results of the different PSF fits on the SM-SERS sample from Figures 4 and 5. Again, it is seen that the dipole PSF fits all show good agreement when fitting the in-plane orientation of the dimer (Figure 4A),  $\varphi$ , just as in the MM-SERS case. In this case, the three-dipole fits show a significantly better agreement with the measured  $\theta$  value of 86° than the one-dipole fit. As in the case of MM-SERS emission, the one-dipole PSF highly overestimates the emission wavelength (based on the MM-SERS spectrum shown in Figure 3B). The three-dipole fit also overestimates  $\lambda$ , although not as dramatically as the one-dipole fit, consistent with previous results. Unlike the MM-SERS case, the 3- $\lambda$  model provides very poor wavelength fits, with both the TM and OOP mode far to the red of the calculated LM emission. Also, by including a  $z$ -offset in the three-dipole model PSF, we again find the most reasonable prediction of the emission wavelength, but also observe an overestimation of the distance of the emission from the surface, as the  $z$ -offset is calculated at  $80 \pm 12$  nm from the surface, while the height of the tallest particle in the dimer is only 59 nm. Finally, we have included the results of the nanoparticle luminescence-subtracted fit, which shows that while there may be a slight difference between the average luminescence-subtracted and unsubtracted three-dipole fit centroids, the other fit estimates are in agreement.

Looking at the calculated centroid values across the different models, we see that the standard deviations

are much higher for the SM-SERS centroid positions (2–4 nm) compared to the MM-SERS values ( $\leq 0.5$  nm). On first glance, one might assume that the larger error is due to lower signal-to-noise associated with SM-SERS, but a comparison across multiple samples found that MM-SERS samples with similar signal-to-noise ratios showed smaller standard deviations in the centroid positions (see Figure S3). Thus, we attribute the increased variability in the centroid position in the SM-SERS sample to an effect of molecular motion, which influences how the molecule interacts with the various plasmon modes of the nanoparticle, thereby shifting its centroid.<sup>6,7,35</sup>

To compare the calculated centroids between MM-SERS and SM-SERS samples, we calculated two-dimensional spatial intensity maps, which relate the intensity of the measured SERS to the position of the calculated centroid.<sup>8</sup> To do this, fitted centroid locations from individual image frames associated with SERS emission are collected into 1 nm bins, and the color of the bin is determined by the average fitted intensity of the points in each bin. We have calculated spatial intensity maps using both the 2-D Gaussian (Figure 6, middle column) and the three-dipole (Figure 6, right column) models. A white “ $\times$ ” is used to represent the average value of the Gaussian centroid in the three-dipole spatial intensity maps for ease of comparison. We chose the single- $\lambda$  three-dipole model with no  $z$ -offset for these calculations because the one-dipole model has provided the poorest fits of all the dipole models, the 3- $\lambda$  model produced unreasonable wavelength values for the TM and OOP modes in the SM-SERS regime, and the three-dipole z-fit model produced nonphysical offset values and poor convergence characteristics.

Figure 6 shows a series of AFM images and the associated spatial intensity maps for three SM-SERS samples and two MM-SERS samples. In the case of the SM-SERS examples (Figure 6, panels A–I), not only do the Gaussian and three-dipole fits localize the emission to different positions, but the three-dipole fits also show significantly more spread in the centroid position, oriented along the  $\varphi$  axis of the dimer. This

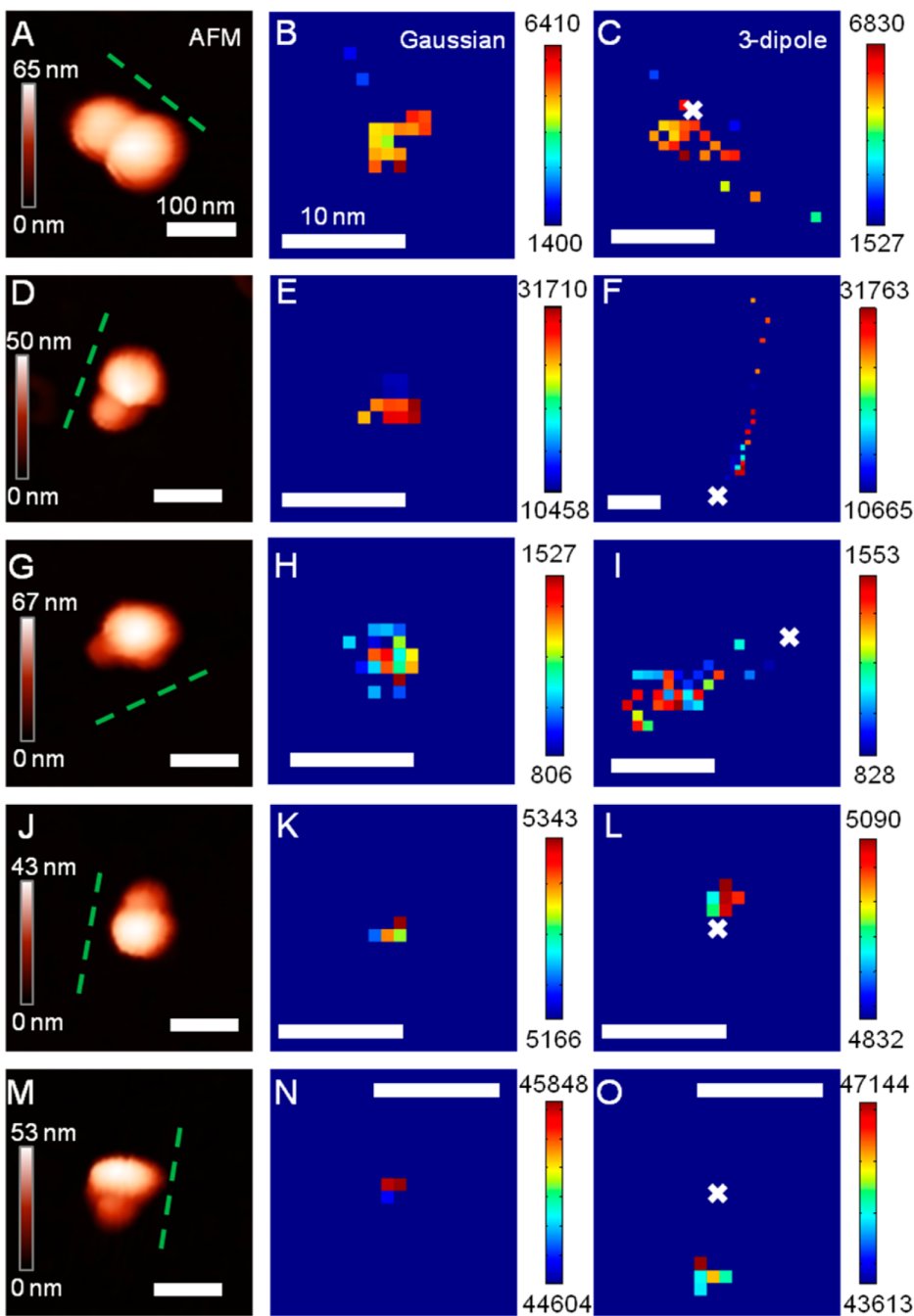


**Figure 6.** AFM images and spatial intensity maps that indicate the average intensity of all centroids located within each 1 nm bin. (Left column) AFM image (with the three-dipole  $\varphi$ -fit estimate indicated by the dashed line), (center column) spatial intensity map using the 2-D Gaussian model, and (right column) spatial intensity map using the three-dipole model. A white  $\times$  indicates the average position of the 2-D Gaussian centroid. Panels A–I show SM-SERS examples, with MM-SERS examples in J–O.

direction of centroid motion is highly correlated with changing values of  $\theta$  (Figure S-7), and consequently we have noted higher uncertainties in the fit values of  $\theta$  in the single-molecule examples (typically  $\pm 3^\circ$ ). As described above, we assign the changing SM-SERS centroid to a mobile molecule on the nanoparticle surface; as the molecule moves, the efficiency with which it couples to the different plasmon modes of the nanoparticle changes, thereby shifting the measured centroid.<sup>6–8</sup> In previous work, we have noted that the

SM-SERS centroid position can change by as much as 40 nm over the course of an experiment, allowing us to effectively map out the local electromagnetic enhancement associated with the hot spot.<sup>8,10</sup> One question that has come up is whether the dramatic change in the centroid position was an artifact due to the relative simplicity of the 2-D Gaussian fitting model we used. In this study, we find that using a more complex three-dipole model actually generates more spread in the centroid position relative to the 2-D Gaussian.

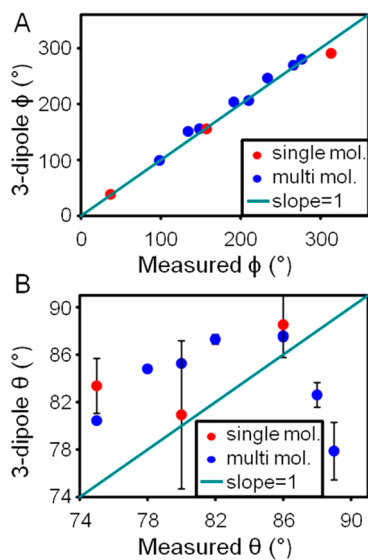


**Figure 7. Relationship between three-dipole fits and estimates based on structure for both (A)  $\phi$  and (B)  $\theta$ . Points are color-coded based on whether the sample is SM- or MM-SERS.**

Moreover, our previous work using a 2-D Gaussian model has shown excellent qualitative agreement between the shape of the spatial intensity maps and the structure of the underlying nanoparticle junctions.<sup>10,36</sup> In the examples shown here, we find that the three-dipole model does not provide good qualitative agreement with the orientation of the nanoparticle junction, suggesting that this model may not completely represent the contributing radiative dipole modes of the nanostructure.

In contrast to the SM-SERS examples, the MM-SERS data shown in Figure 6, panels J–O, show tightly confined centroid positions associated with low standard deviations in the calculated  $\theta$  values ( $\pm 0.7^\circ$ ). The MM-SERS centroid behavior is consistent with the picture that we are measuring an ensemble-averaged centroid position, due to the fact that we have multiple molecules that are able to couple to most/all resonant plasmon modes within the structure. Even if the molecules are mobile on the surface, the average centroid does not change dramatically because the high surface coverage ensures that emission is not dominated by coupling to a single plasmon mode. As a result, the centroid collapses to a single value, which is largely dictated by the geometry of the nanostructure, rather than the positions of the individual molecules.

Despite the fact that the SM-SERS samples show mobile centroids relative to the MM-SERS counterparts, we find that the three-dipole fit is still able to produce orientation parameters that reflect the underlying nanoparticle structure. In Figure 7, we show the relationship between the measured and fit values of both  $\phi$  and  $\theta$  using the three-dipole PSF. In Figure 7A, the calculated  $\phi$  value agrees well with the experimentally measured  $\phi$  value based on the nanoparticle

structure whether we are probing an SM-SERS- or an MM-SERS-active dimer. However, when comparing  $\theta$ -fit values with the measured structure of the nanoparticle (Figure 7B), we see that the fit data do not agree with the measured structure as well as the  $\phi$  values do (AFM images of all aggregates in Figure 7 are shown in Figure S1). The lack of agreement may be due to our definition of  $\theta$ , which is based on the relative height and separation of the two nanoparticles and may not reflect the true orientation of the longitudinal plasmon mode. We also observe that the single molecule cases have larger uncertainties in  $\theta$  than the MM-SERS cases, consistent with the larger centroid uncertainties noted in Figure 6. We again attribute the increased uncertainty in  $\theta$  to an effect from the motion of a single molecule, whereas molecular effects in the case of the high-dye-concentration samples are averaged over many molecules.

After comparing the quality of super-resolution fits using both Gaussian and dipole emission PSF modeling, we find that none of the dipole PSFs used in this study can accurately describe the full PSF of a SERS-active aggregate, based on the nonrandom residuals associated with the various fits. This being said, a three-dipole PSF fit showed much lower residuals than the 2-D Gaussian and was able to accurately represent the geometry of the underlying structure, while still being sensitive to the contributions of the molecule in the SM-SERS examples. Even for the simple case of nanoparticle dimers, the minimum level of complexity that can give reasonable estimates for  $\theta$  and  $\lambda$  is a three-dipole fit. Fitting plasmon-mediated emission with a dipole PSF of insufficient complexity (e.g., a one-dipole fit) can strongly skew several fit parameters, notably  $\theta$ ,  $\lambda$ , and the centroid location.

We hypothesize that one reason the three-dipole fits show systematic residuals in both the MM-SERS and SM-SERS cases is that the three mutually orthogonal dipoles share a common origin. In reality, we would not expect this to be the case. For example, an asymmetric dimer is expected to have a longitudinal dipole mode oriented along the long axis of the dimer, as well as two transverse modes, each associated with the two different nanoparticles that comprise the dimer. If the two nanoparticles are of different size (as is the case in the examples shown here), then we expect one transverse mode to have a stronger resonant overlap with our emission than the other,<sup>37</sup> which would bias the origin of the emission polarized along the transverse dipole mode toward one nanoparticle. Our three-dipole model cannot capture this subtle shift because we model the three dipoles as originating from a common origin, which may explain why our fits still show systematic errors. In principle, we could try to fit the data to three (or more) decoupled dipole modes, but the number of adjustable parameters becomes quite high and the computational expense nearly prohibitive. Moreover,

as we work on higher order aggregates (trimers, tetramers, etc.), representing the various mode contributions (especially in the absence of structure correlation) becomes extremely challenging. While the dipole models yield insight into the nature of the underlying plasmon modes and provide a more physical representation of the coupled molecule–nanoparticle system, the 2-D Gaussian still remains a useful and complementary model in super-resolution fitting of plasmon-mediated emission, due to its robustness, low computational expense, and ability to capture the effect of a mobile molecule on the centroid position in SM-SERS samples.

## CONCLUSION

In this study, we have compared the results of fitting diffraction-limited emission patterns from both MM-SERS- and SM-SERS-active silver nanoparticle dimers, using a 2-D Gaussian and several variations of a dipolar emission PSF. A three-dipole PSF fit provided the best

overall fit, based on the magnitude of the residuals and fits to measurable parameters ( $\varphi$ ,  $\theta$ ,  $\lambda$ ), although with increased computational expense, systematic error in the fits, and imperfect agreement between the structure of the nanoparticle and the shape of the spatial intensity maps in the SM-SERS limit. We have also shown that, based on the difference between the SM-SERS and MM-SERS examples, the position of the SERS reporter molecule can influence the shape of the PSF—and thus the results of the fit—in the low-concentration regime. On the other hand, a high concentration of SERS reporter molecules yields less uncertainty in the fit parameters and gives more precise centroid localization, due to the averaging of the various molecular contributions to the PSF. Lastly, we show that the choice of model when fitting plasmon-mediated emission strongly affects super-resolution results and that structure correlation remains an important tool for comparing spatial intensity maps against nanoparticle geometry.

## METHODS

**Sample Preparation.** Colloidal silver nanoparticles were prepared using previously published methods and were used as prepared.<sup>38</sup> Aliquots of the colloidal silver solution (either 1 mL or 100  $\mu$ L) were mixed with R6G and NaCl solutions to final concentrations of approximately either 2 or 200 nM R6G for the SM-SERS and MM-SERS samples, respectively (yielding roughly 2 or 200 R6G molecules per nanoparticle dimer).<sup>6,8,10,38</sup> The final concentration of NaCl in both samples was 10 mM. In the case of MM-SERS samples, solutions were centrifuged for 10 min at  $\sim$ 500g and then resuspended in 10 mM NaCl to form an 8 $\times$  dilution before drop-casting, in order to remove excess R6G.<sup>28</sup> The SM-SERS sample was diluted 1:1 with ultrapure H<sub>2</sub>O before drop-casting. In order to facilitate AFM correlation, alphanumerically gridded #1 glass coverslips were used as a sample substrate.<sup>10</sup> Slides were cleaned for 10 min in an argon plasma and were then incubated in a  $\sim$ 0.5% by volume solution of either aminopropyltriethoxysilane or aminopropyltrimethoxysilane in ethanol for 10 min. Sample slides were prepared by drop-casting 5  $\mu$ L of SERS solution onto the slide for several seconds, then drying with a gentle stream of nitrogen. Next, 5  $\mu$ L of a diluted sample of 500 nm diameter Spherotech Sky Blue fluorescent beads was drop-cast and allowed to sit for 5 min before gently rinsing with ultrapure H<sub>2</sub>O. Samples were stored in the dark in a vacuum desiccator when not being imaged or undergoing AFM.

**Optical Experiments and Structure Correlation.** Optical measurements were carried out using an Olympus IX-71 inverted optical microscope equipped with a 1.3 variable NA, 100 $\times$ , oil immersion objective, an electron-multiplied CCD detector (ProEM, Princeton Instruments) for super-resolution imaging, and a liquid nitrogen-cooled CCD/spectrometer system (Princeton Instruments Spec-10/Acton SpectraPro 2500i) for simultaneous collection of spectra. Experiments were performed under quasi-circularly polarized 532 nm excitation in an epi-illumination configuration at irradiances of approximately 480–800 W/cm<sup>2</sup>. Integration times were 100 ms/1 s in MM-SERS experiments and 200 ms/2 s in SM-SERS experiments for images/spectra. Dark-field spectra were collected using a tungsten light source passed through a dark-field condenser, and low-angle scattered light was collected by lowering the adjustable NA of the objective. MM-SERS experiments were carried out in both ambient and dry nitrogen environments, and no difference was observed between the two systems. SM-SERS experiments

were performed in ambient air only. AFM correlation was carried out after the optical experiments by transferring the gridded slide to a combined AFM–total internal reflection optical microscope as described previously.<sup>29,39</sup>

**Image Processing.** For each SERS-active aggregate, 20–40 image frames were analyzed out of the full-length experimental image stack, due to fit time considerations. Intensity *versus* time plots and spectra are included in SI section S2, showing which regions were included for analysis for the SM-SERS examples. For 2-D Gaussian fitting, we utilized in-house MATLAB code as described previously.<sup>8,10,13</sup> The dipole emission PSF code was created using a modified version of Jörg Enderlein's "QDControl.m" code, which he has made available online.<sup>33</sup> As in previous studies, the selection between 1/3-dipole fits was accomplished *via* fixing the  $R$  and  $\kappa$  parameters in the fit.<sup>30</sup> The 3- $\lambda$  dipole PSF fit was carried out by combining three one-dipole PSFs in a single fit simultaneously, where each component of the fit was restricted to have the same centroid and each dipole was fixed to be orthogonal to the other two.<sup>30</sup> Once the PSF models were constructed, fits were carried out using a bounded least-squares fitting algorithm in MATLAB.

**Conflict of Interest:** The authors declare no competing financial interest.

**Supporting Information Available:** AFM images of all MM- and SM-SERS dimers used in this study, intensity *versus* time plots and spectra for the SM-SERS examples, and plots comparing the SERS signal-to-noise ratio to the uncertainty in the fitted  $\theta$  values. This material is available free of charge *via* the Internet at <http://pubs.acs.org>.

**Acknowledgment.** The authors would like to thank M. Weber and Y. Mueanngern for preparing the Ag colloids used in this study and J. Enderlein for freely distributing his "QDControl.m" code through his Web site. This material is based on work supported by the Welch Foundation under Award No. F-1699.

## REFERENCES AND NOTES

1. Hao, E.; Schatz, G. C. Electromagnetic Fields around Silver Nanoparticles and Dimers. *J. Chem. Phys.* **2004**, *120*, 357–366.
2. Halas, N. J.; Lal, S.; Chang, W.-S.; Link, S.; Nordlander, P. Plasmons in Strongly Coupled Metallic Nanostructures. *Chem. Rev.* **2011**, *111*, 3913–3961.

3. Etchegoin, P. G.; Le Ru, E. C. A Perspective on Single Molecule SERS: Current Status and Future Challenges. *Phys. Chem. Chem. Phys.* **2008**, *10*, 6079.
4. Michaels, A. M.; Jiang, J.; Brus, L. Ag Nanocrystal Junctions as the Site for Surface-Enhanced Raman Scattering of Single Rhodamine 6G Molecules. *J. Phys. Chem. B* **2000**, *104*, 11965–11971.
5. Camden, J. P.; Dieringer, J. A.; Wang, Y.; Masiello, D. J.; Marks, L. D.; Schatz, G. C.; Van Duyne, R. P. Probing the Structure of Single-Molecule Surface-Enhanced Raman Scattering Hot Spots. *J. Am. Chem. Soc.* **2008**, *130*, 12616–12617.
6. Titus, E. J.; Weber, M. L.; Stranahan, S. M.; Willets, K. A. Super-Resolution SERS Imaging beyond the Single-Molecule Limit: An Isotope-Edited Approach. *Nano Lett.* **2012**, *12*, 5103–5110.
7. Ausman, L. K.; Schatz, G. C. On the Importance of Incorporating Dipole Reradiation in the Modeling of Surface Enhanced Raman Scattering from Spheres. *J. Chem. Phys.* **2009**, *131*, 084708–084708–10.
8. Stranahan, S. M.; Willets, K. A. Super-Resolution Optical Imaging of Single-Molecule SERS Hot Spots. *Nano Lett.* **2010**, *10*, 3777–3784.
9. Weber, M. L.; Willets, K. A. Nanoscale Studies of Plasmonic Hot Spots Using Super-Resolution Optical Imaging. *MRS Bull.* **2012**, *37*, 745–751.
10. Weber, M. L.; Willets, K. A. Correlated Super-Resolution Optical and Structural Studies of Surface-Enhanced Raman Scattering Hot Spots in Silver Colloid Aggregates. *J. Phys. Chem. Lett.* **2011**, *2*, 1766–1770.
11. Willets, K. A.; Stranahan, S. M.; Weber, M. L. Shedding Light on Surface-Enhanced Raman Scattering Hot Spots through Single-Molecule Super-Resolution Imaging. *J. Phys. Chem. Lett.* **2012**, *3*, 1286–1294.
12. Yildiz, A.; Forkey, J. N.; McKinney, S. A.; Ha, T.; Goldman, Y. E.; Selvin, P. R. Myosin V Walks Hand-over-Hand: Single Fluorophore Imaging with 1.5-nm Localization. *Science* **2003**, *300*, 2061–2065.
13. Blythe, K. L.; Mayer, K. M.; Weber, M. L.; Willets, K. A. Ground State Depletion Microscopy for Imaging Interactions Between Gold Nanowires and Fluorophore-Labeled Ligands. *Phys. Chem. Chem. Phys.* **2013**, *15*, 4136–4145.
14. Lin, H.; Centeno, S. P.; Su, L.; Kenens, B.; Rocha, S.; Sliwa, M.; Hofkens, J.; Uji-i, H. Mapping of Surface-Enhanced Fluorescence on Metal Nanoparticles Using Super-Resolution Photoactivation Localization Microscopy. *ChemPhysChem* **2012**, *13*, 973–981.
15. Zhou, X.; Andoy, N. M.; Liu, G.; Choudhary, E.; Han, K.-S.; Shen, H.; Chen, P. Quantitative Super-Resolution Imaging Uncovers Reactivity Patterns on Single Nanocatalysts. *Nat. Nanotechnol.* **2012**, *7*, 237–241.
16. Cang, H.; Labno, A.; Lu, C.; Yin, X.; Liu, M.; Gladden, C.; Liu, Y.; Zhang, X. Probing the Electromagnetic Field of a 15-Nanometre Hotspot by Single Molecule Imaging. *Nature* **2011**, *469*, 385–388.
17. Wei, L.; Liu, C.; Chen, B.; Zhou, P.; Li, H.; Xiao, L.; Yeung, E. S. Probing Single-Molecule Fluorescence Spectral Modulation within Individual Hotspots with Subdiffraction-Limit Image Resolution. *Anal. Chem.* **2013**, *85*, 3789–3793.
18. Willets, K. A. Plasmon Point Spread Functions: How Do We Model Plasmon-Mediated Emission Processes? *Front. Phys.* **2013**, *1*, 1–14.
19. Enderlein, J.; Toprak, E.; Selvin, P. R. Polarization Effect on Position Accuracy of Fluorophore Localization. *Opt. Express* **2006**, *14*, 8111–8120.
20. Engelhardt, J.; Keller, J.; Hoyer, P.; Reuss, M.; Staudt, T.; Hell, S. W. Molecular Orientation Affects Localization Accuracy in Superresolution Far-Field Fluorescence Microscopy. *Nano Lett.* **2011**, *11*, 209–213.
21. Lew, M. D.; Backlund, M. P.; Moerner, W. E. Rotational Mobility of Single Molecules Affects Localization Accuracy in Super-Resolution Fluorescence Microscopy. *Nano Lett.* **2013**.
22. Bartko, A. P.; Dickson, R. M. Three-Dimensional Orientations of Polymer-Bound Single Molecules. *J. Phys. Chem. B* **1999**, *103*, 3053–3056.
23. Bartko, A. P.; Dickson, R. M. Imaging Three-Dimensional Single Molecule Orientations. *J. Phys. Chem. B* **1999**, *103*, 11237–11241.
24. Böhmer, M.; Enderlein, J. Orientation Imaging of Single Molecules by Wide-Field Epifluorescence Microscopy. *J. Opt. Soc. Am. B* **2003**, *20*, 554–559.
25. Backlund, M. P.; Lew, M. D.; Backer, A. S.; Sahl, S. J.; Grover, G.; Agrawal, A.; Piestun, R.; Moerner, W. E. Simultaneous, Accurate Measurement of the 3D Position and Orientation of Single Molecules. *Proc. Natl. Acad. Sci.* **2012**, *109*, 19087–19092.
26. Li, Z.; Shegai, T.; Haran, G.; Xu, H. Multiple-Particle Nanantennas for Enormous Enhancement and Polarization Control of Light Emission. *ACS Nano* **2009**, *3*, 637–642.
27. Shegai, T.; Li, Z.; Dadash, T.; Zhang, Z.; Xu, H.; Haran, G. Managing Light Polarization via Plasmon–Molecule Interactions within an Asymmetric Metal Nanoparticle Trimer. *Proc. Natl. Acad. Sci.* **2008**, *105*, 16448–16453.
28. Shegai, T.; Brian, B.; Miljković, V. D.; Käll, M. Angular Distribution of Surface-Enhanced Raman Scattering from Individual Au Nanoparticle Aggregates. *ACS Nano* **2011**, *5*, 2036–2041.
29. Stranahan, S. M.; Titus, E. J.; Willets, K. A. SERS Orientational Imaging of Silver Nanoparticle Dimers. *J. Phys. Chem. Lett.* **2011**, *2*, 2711–2715.
30. Titus, E. J.; Willets, K. A. Accuracy of Superlocalization Imaging Using Gaussian and Dipole Emission Point-Spread Functions for Modeling Gold Nanorod Luminescence. *ACS Nano* **2013**, *7*, 6258–6267.
31. Dieringer, J. A.; Lettan, R. B.; Scheidt, K. A.; Van Duyne, R. P. A Frequency Domain Existence Proof of Single-Molecule Surface-Enhanced Raman Spectroscopy. *J. Am. Chem. Soc.* **2007**, *129*, 16249–16256.
32. Nie, S.; Emory, S. R. Probing Single Molecules and Single Nanoparticles by Surface-Enhanced Raman Scattering. *Science* **1997**, *275*, 1102–1106.
33. Enderlein, J. *Imaging of Single Molecules*. <http://www.joerg-enderlein.de/imagingOfSingleMolecules.html> (accessed May 3, 2013).
34. Hellen, E. H.; Axelrod, D. Fluorescence Emission at Dielectric and Metal-Film Interfaces. *J. Opt. Soc. Am. B* **1987**, *4*, 337–350.
35. Stranahan, S. M.; Titus, E. J.; Willets, K. A. Discriminating Nanoparticle Dimers from Higher Order Aggregates through Wavelength-Dependent SERS Orientational Imaging. *ACS Nano* **2012**, *6*, 1806–1813.
36. Weber, M. L.; Litz, J. P.; Masiello, D. J.; Willets, K. A. Super-Resolution Imaging Reveals a Difference between SERS and Luminescence Centroids. *ACS Nano* **2012**, *6*, 1839–1848.
37. Oubre, C.; Nordlander, P. Optical Properties of Metallodielectric Nanostructures Calculated Using the Finite Difference Time Domain Method. *J. Phys. Chem. B* **2004**, *108*, 17740–17747.
38. Lee, P. C.; Meisel, D. Adsorption and Surface-Enhanced Raman of Dyes on Silver and Gold Sols. *J. Phys. Chem.* **1982**, *86*, 3391–3395.
39. Kaplan-Ashiri, I.; Titus, E. J.; Willets, K. A. Subdiffraction-Limited Far-Field Raman Spectroscopy of Single Carbon Nanotubes: An Unenhanced Approach. *ACS Nano* **2011**, *5*, 1033–1041.